sensors

Article

Space Robot Sensor Noise Amelioration Using Trajectory Shaping

Emily Kuck [1] **and Timothy Sands** [2,*]

[1] Sibley School of Mechanical and Aerospace Engineering, Cornell University, Ithaca, NY 14853, USA; epk37@cornell.edu
[2] Department of Mechanical Engineering (SCPD), Stanford University, Stanford, CA 94305, USA
* Correspondence: dr.timsands@alumni.stanford.edu

Abstract: Robots in space are necessarily extremely light and lack structural stiffness resulting in natural frequencies of resonance so low as to reside inside the attitude controller's bandwidth. A variety of input trajectories can be used to drive a controller's attempt to ameliorate the control-structural interactions where feedback is provided by low-quality, noisy sensors. Traditionally, step functions are used as the ideal input trajectory. However, step functions are not ideal in many applications, as they are discontinuous. Alternative input trajectories are explored in this manuscript and applied to an example system that includes a flexible appendage attached to a rigid main body. The main body is controlled by a reaction wheel. The equations of motion of the flexible appendage, rigid body, and reaction wheel are derived. A benchmark feedback controller is developed to account for the rigid body modes. Additional filters are added to compensate for the system's flexible modes. Sinusoidal trajectories are autonomously generated to feed the controller. Benchmark feedforward whiplash compensation is additionally implemented for comparison. The method without random errors with the smallest error is the sinusoidal trajectory method, which showed a 97.39% improvement when compared to the baseline response when step trajectories were commanded, while the sinusoidal method was inferior to traditional step trajectories when sensor noise and random errors were present.

Keywords: structural dynamics; flexible robotics; bandpass filter; notch filter; structural filtering; trajectory generation; whiplash compensation

check for updates

Citation: Kuck, E.; Sands, T. Space Robot Sensor Noise Amelioration Using Trajectory Shaping. *Sensors* **2024**, *24*, 666. https://doi.org/10.3390/s24020666

Academic Editors: Andrey V. Savkin and Aiguo Song

Received: 29 November 2023
Revised: 3 January 2024
Accepted: 18 January 2024
Published: 20 January 2024

1. Introduction

The solutions and methods developed in this manuscript are applicable to a wide range of dynamics problems. A robotic arm is chosen here as an example of a highly flexible system, with implications across the industry. Robots are deployed in space for a variety of purposes. Figure 1a shows one such robot, NASA's Robonaut 2. In addition to space applications, robotic arms can be deployed underwater, as evidenced by Figure 1b. Whether in space or underwater, the commanded trajectory can influence the tracking error of the robotic arm.

Minimizing tracking error can allow for more precise movements and support the execution of detailed motion. In-orbit servicing is an example of the need for precise control over a robotic arm's movement. By identifying the most appropriate trajectory to command, the error in angular movement can be minimized.

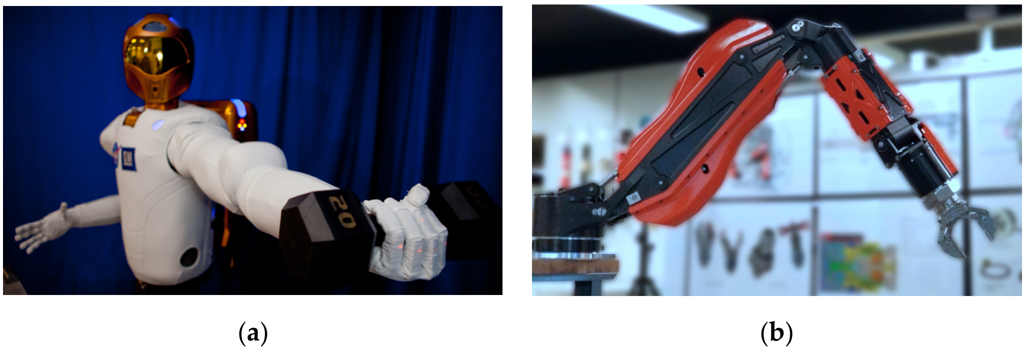
(a) (b)

Figure 1. (**a**) NASA's Robonaut 2, built at Johnson Space Center, became the first android astronaut to go to space in 2011. Now, about two dozen former NASA engineers, many of whom helped build the robot astronaut, have turned their skills to creating underwater robots at Nauticus Robotics [1]; (**b**) Nauticus is also commercializing the robotic arm technology–known as Olympic Arm–that it developed while designing and building Aquanaut. Image credits (both): Nauticus Robotics Inc., Webster, IA, USA [1] used in compliance with image use policy [2], "NASA content (images, videos, audio, etc.) are generally not copyrighted and may be used for educational or informational purposes without needing explicit permissions".

Towards in–orbit servicing, the importance of spacecraft-mounted robotics missions is highlighted in reference [3] which stipulates:

> ". . .environmental, economic, and strategic considerations support the claim that the future of a space infrastructure will depend on the ability to perform on-orbit servicing, encompassing a broad array of in-space operations, such as inspection, berthing, refueling, repair, assembly, and so on."

According to a 2010 study by the U.S. National Air and Space Administration (NASA), [4] a key to enabling robotic servicing missions in space leading to advantageous future strategic impact, cost effectiveness, and environmental sustainability. Cost effectiveness is manifest in the ability to relatively cheaply replace spacecraft components rather than launch a replacement spacecraft. Reference [5] indicates since 1957 roughly 5400 space missions have been flown, while nearly twenty-thousand space objects are tracked by the north American air defense command (NORAD), where over two thousand are rocket upper stages spent of fuel and over ten thousand additional items are classified as debris. Current proposals [6,7] indicate intentions for very large future constellations together comprising another twenty thousand objects in orbit. Such a large number of craft in orbit constitute a potentially lucrative business model for system repair [8] and refueling on-orbit. Discovery of the very origins of life and human long-term habitability are postulated to be aided by space robotics in [9].

This manuscript investigates the importance of the trajectory shaping fed to the control method used to rotate the space robot. The flexible spacecraft system examined in this manuscript is indicative of a larger dynamics problem. The solutions and methods explored are applicable to that larger set of dynamic problems. The requisite equations of motion are derived and feedback controllers and second-order structural filters are applied, following the methodology developed in [10]. Initially, sinusoidal trajectory generation is used to drive the controllers. Whiplash compensation is additionally investigated as a solution, per [11]. Three methods of trajectory shaping are applied to the flexible spacecraft robotic system and compared critically: step shaped, sinusoidally shaped, and whiplash shaped. The state errors, rate errors, and control efforts are compared for each of the three methods of input control to determine which is most appropriate for the flexible spacecraft system application.

Elder techniques for controlling highly flexible systems relied foremost on feedback necessitating construction of feedback linearizing control laws [12]. The linear-quadratic regulator approach, robust control approaches minimizing the $H\infty$ and H2 norms, and a disparate approach based in analytical dynamics, introduced as the Udwadia–Kalaba approach were compared in reference [13]. Very recently, integration of fuel slosh with centralized sensors and actuators, without the usage of collocated devices for vibration management. into techniques to control the motion of flexible appendages was offered by [14] reiterating the relevance of classical proportional, derivative (PD) control with nonadaptive bandpass filters, where the novel proposition includes integration of wave-based control with the filtered PD control scheme. Vibration suppression was illustrated by establishing a dynamic grasping area to describe the contact procedure of the capture device grasping target in reference [15]. Control of rotation-floating space robots with flexible appendages specifically for on-orbit servicing was proposed in [16]. Techniques were suggested using a composite two-time-scale control system [17]. Open-loop methods were strictly used for analysis while closed-loop was utilized for control in reference [18]. Another alternative is adaptive feedback control [19].

The following list highlights the current state of the art developing deterministic artificial intelligence:

1. In 2019, reference [11] revealed an optimal control revealed by pseudospectral optimization software where the solution validation was provided using six theoretical necessary conditions of optimization: (1) Hamiltonian minimization condition; (2) adjoint equations; (3) terminal transversality condition; (4) Hamiltonian final value condition; (5) Hamiltonian evolution equation; and lastly (6) Bellman's principle. The results are novel and unique in that they initially command full control in the opposite direction from the desired end state, while no such results are seen using classical control methods including classical methods augmented with structural filters typically employed for controlling highly flexible multi-body systems.
2. Later in 2022, an interesting study of the use of feedback and structural filtering to maximize system stability was offered [10], leading to the recommendation to use single-sinusoidal trajectory shaping to maximize stability.

The following brief list articulates the novel growth from the current state of the art methods.

1. Rather than propose options for maximizing stability [10], this study seeks to offer advice to minimize trajectory tracking errors.
2. Rather than focus on feedforward [11] versus feedback [10], this study investigates commanded trajectory tracking options.

This manuscript advises the readership on methods to shape the commanded trajectory to be tracked, where sinusoidal, whiplash, and step trajectories are critically compared using tracking errors (both angle and angular rate) and control effort as figures of merit.

2. Materials and Methods

In this manuscript, the flexible spacecraft system shown in Figure 2 is analyzed. The system consists of a rigid main body R, reaction wheel W, and a flexible appendage F. The flexible appendage F is split into beam elements 1 through 7, and node points 1 through 8. Table 1 lists parameters of the flexible spacecraft system and their descriptions. The methods applied in this section can be used for any dynamic, flexible system and is not limited to spacecraft application. The flexible spacecraft system in Figure 2 is explored in this manuscript as an example.

2.1. Equations of Motion

The equations of motion of the flexible spacecraft system are derived using the Lagrange method. Lagrangian Mechanics requires kinetic and potential energies. See Table 1 for parameter definitions.

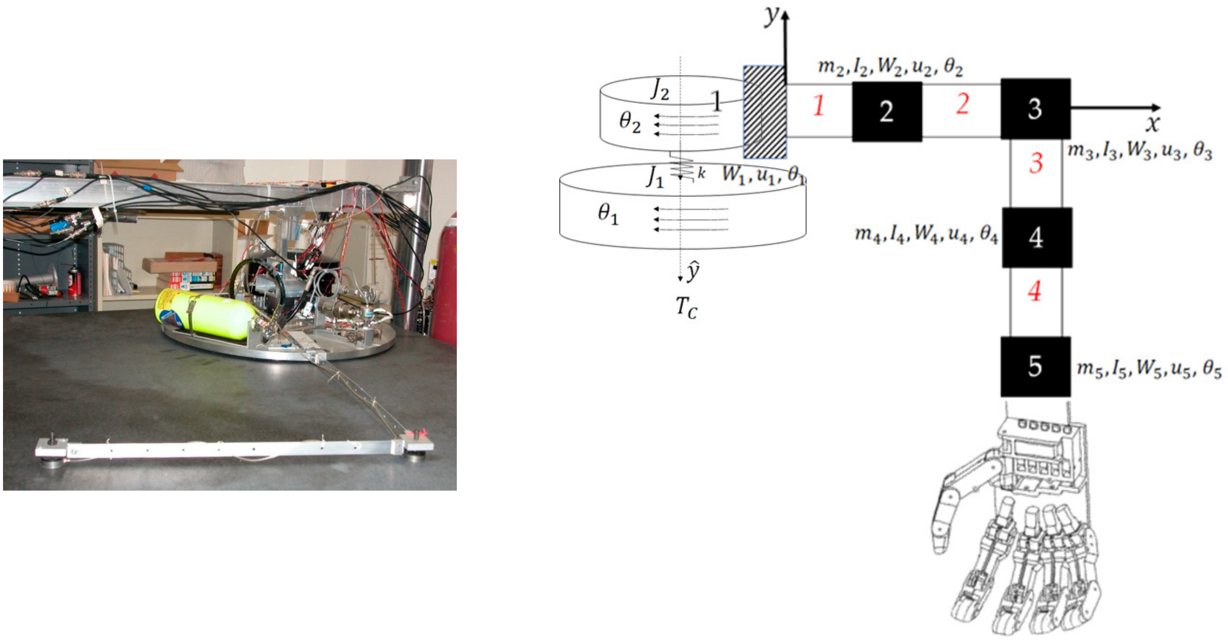

(**a**)

(**b**)

Figure 2. Flexible spacecraft system. (**a**) Atop a (planar) air bearing table, a free-floating space robot is autonomously controlled. [20] Imagery and photographs of the Department of Defense are in the public domain, unless otherwise noted [21]; (**b**) schematic diagram of the free-floating flexible space system depicted in subfigure (**a**). This schematic is identical to that used in references [10,11], where this manuscript comprises the latest iteration of continuing research. No special permission is required to reuse all, or part of the article published by MDPI, including figures and tables [22].

Table 1. Flexible Spacecraft System Parameters.

Variable	Definition	Variable	Definition	Variable	Definition
T	Kinetic energy	T	Natural frequency of i-th mode	V	Potential energy
I_{zz}	Moment of inertia of rigid body	ϕ_i	Modal coordinates	W	Displacement
I_w	Moment of inertia of reaction wheel	x_F	Final position, x	Q	Sheer forces
θ	Angle of flexible appendage	y_F	Final position, y	M	Moments
θ_w	Angle of reaction wheel	n	Number of independent modes	L	Lagrangian
q_i	Modal coordinates	D_i	Elastic decoupling coefficients	T_D	Disturbance torque

The kinetic energy of the entire flexible spacecraft system was found by summing the kinetic energies of the rigid main body, flexible appendage, and reaction wheel. The kinetic energies are written in terms of the moments of inertia and the modal coordinates, as seen in Equation (1). D_i are the rigid-elastic coupling terms and are defined in Equation (2). The modal coordinates are expressed in terms of q and F, which are defined in Equations (4) and (5) for a given beam i.

$$T = \frac{1}{2} I_{zz} \dot{\theta}^2 + \frac{1}{2} I_w \dot{\theta}_w^{\,2} + I_w \dot{\theta} \dot{\theta}_w + \frac{1}{2} \sum_{i=1}^{n} \dot{q}_i + \dot{\theta} \sum_{i=1}^{n} D_i \dot{q}_i \tag{1}$$

The potential energy is shown in Equation (3), where ω_i are the natural frequencies of the flexible spacecraft system for mode i.

$$D_i = \int [x_F {\phi_i}^y - y_F {\phi_i}^x] dm \tag{2}$$

$$V = \frac{1}{2}\sum_{i=1}^{n} {\omega_i}^2 {q_i}^2 \tag{3}$$

$$\{q\} = \{W_1 \quad \theta_1 \quad W_2 \quad \theta_2 \ \}^T \tag{4}$$

$$\{F\} = \{Q_1 \quad M_1 \quad Q_2 \quad M_2 \ \}^T \tag{5}$$

The Lagrange equation, shown in Equation (6) is applied to the Lagrangian L, where $L = T - V$. The Lagrange method results in the equations of motion (EOM) of the flexible spacecraft system, which are shown in Equation (7).

$$\frac{-d}{dt}\left(\frac{\delta L}{\delta \dot{u}_i}\right) - \left(\frac{\delta L}{\delta u_i}\right) = Q_i \tag{6}$$

$$EOM : \begin{cases} I_{zz}\ddot{\theta} + I_w\ddot{\theta}_w + \sum\limits_{i=1}^{n} D_i\dot{q}_i = T_D \\ I_w\left(\ddot{\theta}_w + \ddot{\theta}\right) = T \\ \ddot{q}_i + {\omega_i}^2 D_i\ddot{\theta} = 0 \end{cases} \tag{7}$$

2.2. Natural Frequencies

After reformulating Equation (7) into canonical form elaborated in Equations (19)–(23) in reference [10], the natural frequencies of the flexible spacecraft system were derived using the finite element method and by solving the eigenvalue problem using the stiffness and mass matrices. It was assumed that all displacements are normal, and the system is constrained in Nastran. The stiffness (k) and mass (m) matrices are constructed for each beam element. The individual stiffness and mass matrices are shown for a given beam element i in Equations (8) and (9).

$$\left[k^i\right] = \begin{bmatrix} 12 & 6L & -12 & 6L \\ 6L & 4L^2 & -6L & 2L^2 \\ -12 & -6L & 12 & -6L \\ 6L & 2L^2 & -6L & 4L^2 \end{bmatrix} \tag{8}$$

$$\left[m^i\right] = \begin{bmatrix} 156 & 22L & 54 & -13L \\ 22L & 4L^2 & 13L & -3L^2 \\ 54 & 13L & 156 & -22L \\ -13L & -3L^2 & -22L & 4L^2 \end{bmatrix} \tag{9}$$

The individual stiffness and mass matrices are added by superposition to form the total stiffness and mass matrices respectively, which are presented in the Appendix A. The solution to the eigenvalue problem, presented in Equation (10), provides the natural frequencies and mode shapes of the flexible spacecraft system. Recall the expressions for the rigid–elastic coupling using modal coordinates: in accordance with Equation (2), φ's are mode shapes from finite element analysis using the eigenvalues of K/M (stiffness/mass). The system stiffness matrix is included in Equation (8) and mass matrix in Equation (9) and result in the natural frequencies and mode shapes for the flexible system. The resulting natural frequencies are listed in Table 2, and their corresponding mode shapes can be found in the Appendix A.

Table 2. Natural Frequencies, ω_n for the Flexible Spacecraft System, in rad/s.

1809.46	596.81	43.72	10.22
1415.52	478.77	30.89	2.07
1042.16	419.02	15.77	0.69
774.31	54.87		

2.3. PID Controller

Facilitating the study of input trajectory shaping methods, some control must be benchmarked. While whiplash control from the prequel in reference [11] was selected as the single feedforward control benchmark (to be discussed shortly in Section 2.6), a PID controller with structural filters was chosen as the single benchmark feedback control and was designed to control the motion of the reaction wheel using the procedures in the prequel (Equations (29)–(38) in reference [10]). The PID controller was designed to meet the following specification requirements: 15% overshoot and control bandwidth of 4 rad/s. It is assumed that the natural frequency of the closed loop response is equal to the control bandwidth. The rise time, damping ratio, settling time, and period are calculated according to Equations (10), (11), (12), and (13), respectively.

$$t_r = \frac{1.8}{\omega_n} = \frac{1.8}{4} = 0.45\text{ s} \tag{10}$$

$$\zeta = \frac{-ln(0.15)}{\sqrt{\pi^2 + ln^2(0.15)}} = 0.517 \tag{11}$$

$$t_s = \frac{4.6}{\zeta\omega_n} = \frac{4.6}{0.517 * 4} = 2.22\text{ s} \tag{12}$$

$$T \cong \frac{10}{\zeta\omega_n} = \frac{10}{0.517 * 4} = 4.84 \tag{13}$$

The proportional, integral, and derivative gain values are calculated according to Equations (14)–(16).

$$K_P = I_w\left({\omega_n}^2 + \frac{2\zeta\omega_n}{T}\right) = 1.537 \tag{14}$$

$$K_I = \frac{I_w{\omega_n}^2}{T} = 0.301 \tag{15}$$

$$K_D = I_w\left(\frac{1}{T} + 2\zeta\omega_n\right) = 0.396 \tag{16}$$

The PID controller and the flexible spacecraft system were modeled in MATLAB®, and the simulation results are presented in Section 3.

2.4. Second-Order Structural Filters

After the addition of the PID controller, it was determined that additional filtering was needed to compensate for the system's flexible modes. Additional filtering was added in the form of second-order structural filters. Classical second-order structural filters were designed to compensate for the flexible modes, following the convention defined in Equation (17), where ω_z and ω_p are the frequencies of the zeros and poles respectively and ζ_z and ζ_p are the damping ratios of the zeros and poles. A tutorial elaboration of classical filter design is available in reference [23].

$$\frac{Output(s)}{Input(s)} = \frac{\frac{s^2}{{\omega_z}^2} + \frac{2\zeta_z}{{\omega_z}^2}s + 1}{\frac{s^2}{{\omega_p}^2} + \frac{2\zeta_p}{{\omega_p}^2}s + 1} \tag{17}$$

Equation (17) was used to generate bandpass and notch filters to compensate for the valley and peaks for each of the flexible mode cantilever responses.

2.5. Sinusoidal Trajectory Generation

The feedback controller was commanded by an autonomously generated sinusoidal trajectory to achieve the desired behavior. A piecewise function was created to support the desired quiescent and maneuver times. The generated sinusoid is structured according to Equation (18). Table 3 lists the proximal variable definitions.

$$z = (A - A_0)[1 + \sin(\omega t + \varnothing)] \tag{18}$$

Table 3. Table of proximal variables and nomenclature [1].

Variable/Acronym	Definition	Variable/Acronym	Definition
z	Sinusoidal trajectory	ω	Frequency
A	Desired magnitude	t	Time
A_0	Initial magnitude	$\varnothing$	Phase offset

[1] Such tables are offered throughout the manuscript to aid readability.

The frequency, ω, is directly and inversely proportional to the desired time of the maneuver. By increasing the frequency, a faster maneuver time can be achieved. During the quiescent periods, a constant signal will be applied. The final piecewise trajectory is formed by summing the constant signals during the quiescent periods with the sinusoidal function as it traverses one valley to the next peak. This sinusoidal trajectory generation technique was added to the MATLAB® SIMULINK® project and the results are detailed in Section 3.

2.6. Whiplash Compensation

Whiplash compensation was proposed as a solution to the flexible spacecraft system control problem in [2]. To prevent overshoot, [2] proposed a driving function that creates motion in the opposite direction as the desired final position.

The whiplash compensation trajectory generation scheme was implemented in SIMULINK® and follows the format of Equation (19).

$$z = (A - A_0)[\sin(\omega t + \varnothing)] \tag{19}$$

The flexible spacecraft system was simulated using MATLAB®'s SIMULINK®. A variable-step size was used along with MATLAB®'s automatic solver selection. Figure 3 shows the topography of the flexible spacecraft system SIMULINK® model. The input trajectory options are shown on the left part of the figure and include a sine trajectory, a square wave, and the shaped-whiplash trajectory. The PID controller and second order filters are applied, and have been described in Sections 2.3 and 2.4, respectively. The final rotation angle is examined, and its performance assessed Section 3.

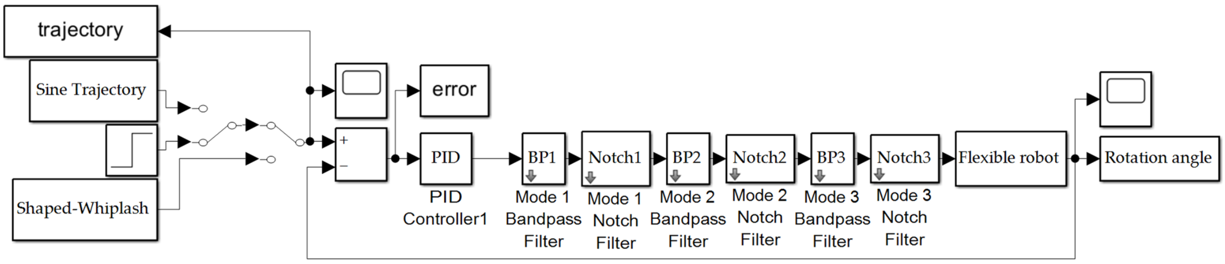

Figure 3. Flexible spacecraft system simulation created in SIMULINK®. Subsystems are displayed in Appendix B.

The state and rate sensor errors are introduced in the SIMULINK® model in order to mimic realistic performance. The state and rate sensor errors are defined by a normally distributed random number with 0 mean and 0.01 variance. The sample time used is 0.01 for the state, rate, and inertia error values. The seed value is generated as a uniformly distributed random number.

The simulation was performed 1000 times for Monte Carlo analysis. Each simulation included the state and rate sensor noises. The Monte Carlo analysis was performed for each of the three trajectory generation schemes: (1) step function, (2) sinusoid trajectory, and (3) whiplash compensation.

3. Results

The various control methods were applied in MATLAB®/SIMULINK® in three different trials, where the following inputs were used to drive the system controller: (1) step response, (2) sinusoidal trajectory, and (3) whiplash compensation. Figure 4 depicts each trajectory as a function of time. The system is expected to complete its maneuver by $t = 5$ s. As seen in Figure 4, the step function has an instantaneous change in value because the step occurs at $t = 0$ s. The sinusoid and whiplash trajectories, on the other hand, are not instantaneous and have a duration. The sinusoid trajectory starts at an amplitude of 0, while the whiplash trajectory starts at an amplitude of -1. The whiplash method generates motion in the opposite direction as the final desired state to prevent overshoot.

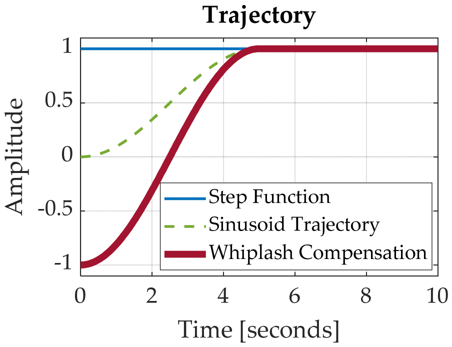

Figure 4. Generated Trajectories.

The flexible spacecraft system is driven by each of the three trajectories in Figure 4. The resulting angle of the reaction wheel is plotted in Figure 5b for all three cases. Similarly, Figure 5c shows the reaction wheel speed error for each controller method. In each figure, the response to a step function input is shown in blue, the response to the generated sinusoid is shown in a dashed green line, and the response to the whiplash compensator is shown in a bolded red line. Figure 5 depicts these results without state and rate sensor noise included.

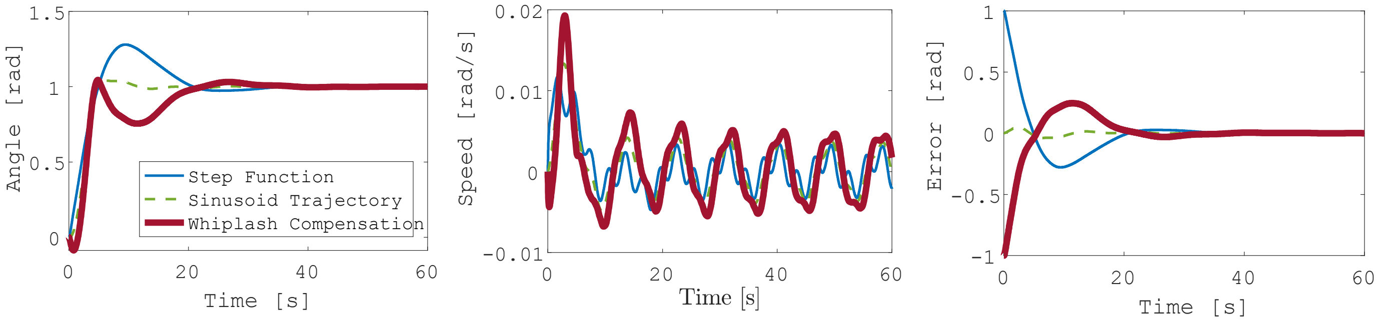

(**a**) (**b**) (**c**)

Figure 5. Generated trajectories (**a**) reaction wheel angle θ; (**b**) reaction wheel speed $\dot{\theta}$; (**c**) reaction wheel rotation angle error.

The mean error value and standard deviation of the error value was calculated and is tabulated in Table 4. Surprisingly, the sinusoid trajectory response shows less error than either the step response or the whiplash response. Monte Carlo simulations were performed for each of the three input trajectory generation schemes. There were 1000 Monte

Carlo trials executed in each simulation. There are two sensor noises included in the model: rotation angle state noise and rotation angle rate noise. Three combinations of noise were included in the Monte Carlo trials: (1) state noise only, (2) rate noise only, and (3) both state and rate noise.

Table 4. Reaction wheel error values. "e−4" notation indicates "$\times 10^{-4}$".

Method	Rotation Angle θ Error Mean	Rotation Angle θ Error Standard Deviation
Step	0.0102	0.2051
Sinusoid	−2.66e−4	0.0141
Whiplash	−0.0145	0.2097

Figure 6 depicts the shotgun plot analysis for each of the noise combinations for the step function input trajectory. Each dot represents one Monte Carlo trial. The one-, two-, and three-sigma ellipses are depicted in red. Table 5 details the mean and standard deviations for each of the methods and combinations of sensor noise.

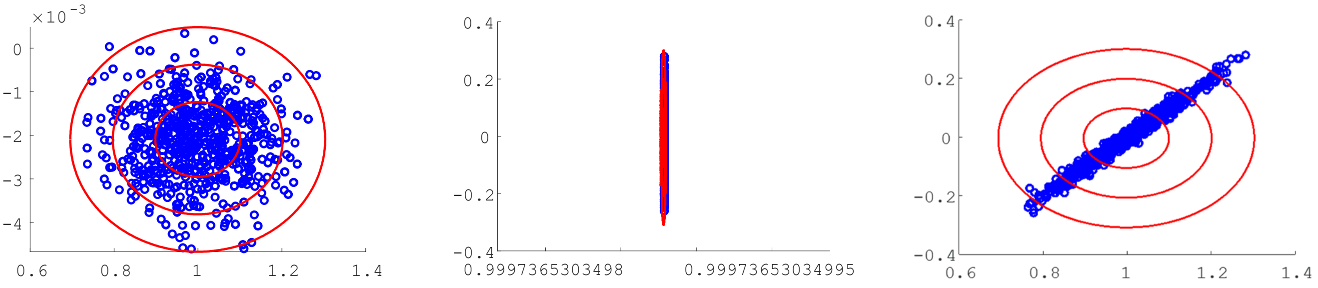

(**a**) (**b**) (**c**)

Figure 6. Monte Carlo analysis of random perturbations for the step function input trajectory, final rotation angle value is on the abscissa and final rotation angle rate value is on the ordinant, each blue dot represents one Monte Carlo trial (**a**) space robot rotation angle in the presence of angle sensor noise; (**b**) space robot rotation rate in the presence of angle rate sensor noise; (**c**) space robot rotation rate in the presence of both angle sensor noise and angle rate sensor noise.

Table 5. Monte Carlo analysis of random perturbations. "e−4" notation indicates "$\times 10^{-4}$".

Method	Rotation Angle θ Error Mean	Rotation Angle θ Error Standard Deviation	Rotation Angle θ Error Mean	Rotation Angle θ Error Standard Deviation	Rotation Angle θ Error Mean	Rotation Angle θ Error Standard Deviation
	With Rotation Angle Sensor Noise		With Rotation Angle Rate Sensor Noise		With Rotation Angle Sensor and Rate Sensor Noise	
Step	−0.0005	−0.0021	−0.0003	−0.0044	−0.0022	−0.0039
Sinusoid	−0.0016	−1.9424e−4	−2.7023e3	16.7673	−0.0025	−0.0019
Whiplash	−0.0007	0.0017	0.0001	−8.8541e−4	−0.0059	−0.0054

4. Discussion

The mean and standard deviation values are compared to the baseline step response error values and tabulated as percentage differences in Table 6. The sinusoid trajectory method shows the most improvement, with an error value 97.39% closer to the desired trajectory than the step response. The whiplash compensation method, on the other hand, proves to be less accurate than the step response, showing a 42.16% increase in mean error.

Table 6. Percent errors for reaction wheel angle.

Method	Rotation Angle θ Error Mean	Rotation Angle θ Error Standard Deviation
Step	---	---
Sinusoid	−97.39%	0.0141
Whiplash	42.16%	0.2097

Driving the flexible spacecraft system with a sinusoidal trajectory is the solution with minimal error when sensor noise is not included. The sinusoidal trajectory generation scheme creates a near step response trajectory, without the discontinuities associated with a step response. The whiplash response is similarly continuous however, it shows more errors than the baseline step response. These results confirm the whiplash solution as a suboptimal result, as was first proposed in [2].

When normally distributed random sensor noise is added to the state and rate sensors, the results align more closely to real world applications. The Monte Carlo simulations performed are summarized in Table 7.

Table 7. Monte Carlo analysis of random perturbations (percent performance improvement).

Method	Rotation Angle θ Error Mean	Rotation Angle θ Error Standard Deviation	Rotation Angle θ Error Mean	Rotation Angle θ Error Standard Deviation	Rotation Angle θ Error Mean	Rotation Angle, θ Error Standard Deviation
	With Rotation Angle Sensor Noise		With Rotation Angle Rate Sensor Noise		With Rotation Angle Sensor and Rate Sensor Noise	
Step	---	---	---	---	---	---
Sinusoid	220.0%	−90.75%	900×10^6%	-381×10^3%	13.64%	−51.28%
Whiplash	40.00%	−181.0%	−133.3%	−79.88%	168.2%	38.46%

5. Conclusions

The whiplash trajectory generation scheme shows a 133.3% improvement when only rate sensor noise is included. The step function method has the least mean error in rotation angle when only the state sensor noise is enabled, as well as when both rate and state sensor noises are enabled.

Without noise included, the sinusoid trajectory shows the most improved performance. However, in the presence of state and rate sensor noises, the step function has the smallest mean error values for the rotation angle. When noise is included, the step function has a 13.64% improvement in mean error when compared to the sinusoid trajectory.

Future research should be conducted to investigate more optimal, continuous trajectory schemes. This could also include investigating the most appropriate solver in MATLAB®. Depending on the solver and step size chosen in MATLAB®'s SIMULINK®, the resulting trajectories could produce different results. Investigating which solver and step size is the most appropriate for this application would render additional confidence in the results. Additionally, more trajectory generation schemes could be evaluated and compared to the sinusoid and whiplash methods. Evaluating additional methods could lead to a more optimal solution with less error.

Author Contributions: Formal analysis, E.K.; investigation, E.K.; conceptualization, T.S.; methodology, T.S.; software, T.S.; validation, T.S.; resources, T.S.; data curation, E.K.; writing—original draft preparation, E.K. and T.S.; writing—review and editing, E.K. and T.S.; visualization, E.K.; supervision, T.S.; project administration, T.S.; funding acquisition, T.S. All authors have read and agreed to the published version of the manuscript.

Funding: This research received no external funding.

Data Availability Statement: To access the data, please contact the corresponding author.

Conflicts of Interest: The authors declare no conflict of interest.

Appendix A

Table A1. Stiffness Matrix, [K]. “e−4” notation indicates “×10^{-4}”.

	W_2	θ_2	W_3	θ_3	W_4	θ_4	W_5	θ_5	u_6	θ_6	u_7	θ_7	u_8	θ_8
W_2	958.818	0	−479.41	59.926	0	0	0	0	0	0	0	0	0	0
θ_2	0	19.975	−59.926	4.9938	0	0	0	0	0	0	0	0	0	0
W_3	−479.41	−59.926	958.82	0	−479.41	59.926	0	0	0	0	0	0	0	0
θ_3	59.926	4.9938	0	19.975	−59.926	4.9938	0	0	0	0	0	0	0	0
W_4	0	0	−479.41	−59.926	958.82	0	−479.41	59.926	0	0	0	0	0	0
θ_4	0	0	59.9260	4.9938	0	19.975	−59.926	4.9938	0	0	0	0	0	0
W_5	0	0	0	0	−479.41	−59.926	479.41	−59.926	0	0	0	0	0	0
θ_5	0	0	0	0	59.926	4.9938	−59.926	19.975	−59.926	4.9938	0	0	0	0
u_6	0	0	0	0	0	0	0	−59.926	958.82	0	−479.41	59.926	0	0
θ_6	0	0	0	0	0	0	0	4.9938	0	19.975	−59.926	4.9938	0	0
u_7	0	0	0	0	0	0	0	0	−479.41	−59.926	958.82	0	479.41	59.926
θ_7	0	0	0	0	0	0	0	0	59.926	4.9938	0	3.39e−5	−59.926	4.9938
u_8	0	0	0	0	0	0	0	0	0	0	−479.41	−59.926	479.41	−59.926
θ_8	0	0	0	0	0	0	0	0	0	0	59.926	4.9938	−59.926	9.9877

Table A2. Mass Matrix, [M]. “e−4” notation indicates “×10^{-4}”.

	W_2	θ_2	W_3	θ_3	W_4	θ_4	W_5	θ_5	u_6	θ_6	u_7	θ_7	u_8	θ_8
W_2	0.4760	0	0.0037	−2.2e−4	0	0	0	0	0	0	0	0	0	0
θ_2	0	3.39e−5	2.2e−4	−1.27e−5	0	0	0	0	0	0	0	0	0	0
W_3	0.0037	2.2e−4	0.4760	0	0.0037	−2.2e−4	0	0	0	0	0	0	0	0
θ_3	−2.2e−4	−1.27e−5	0	3.39e−5	2.2e−4	−1.27e−5	0	0	0	0	0	0	0	0
W_4	0	0	0.0037	2.2e−4	0.4760	0	0.0037	−2.2e−4	0	0	0	0	0	0
θ_4	0	0	−2.2e−4	−1.27e−5	0	3.39e−5	2.2e−4	−1.27e−5	0	0	0	0	0	0
W_5	0	0	0	0	0.0037	2.2e−4	2.63	−3.73e−4	0	0	0	0	0	0
θ_5	0	0	0	0	−2.2e−4	−1.27e−5	−3.73e−4	3.39e−5	2.2e−4	−1.27e−5	0	0	0	0
u_6	0	0	0	0	0	0	0	2.2e−4	0.4760	0	0.0037	−2.2e−4	0	0
θ_6	0	0	0	0	0	0	0	−1.27e−5	0	3.39e−5	2.2e−4	−1.27e−5	0	0
u_7	0	0	0	0	0	0	0	0	0.0037	2.2e−4	0.4760	0	0.0037	−2.2e−4
θ_7	0	0	0	0	0	0	0	0	−2.2e−4	−1.27e−5	0	3.39e−5	2.2e−4	−1.27e−5
u_8	0	0	0	0	0	0	0	0	0	0	0.0037	2.2e−4	0.4660	−3.73e−4
θ_8	0	0	0	0	0	0	0	0	0	0	−2.2e−4	−1.27e−5	−3.73e−4	1.69e−5

Table A3. Mode Shapes for each Natural Frequency. “e−4” notation indicates “$\times 10^{-4}$”.

1.07e−4	−2.55e−4	−2.32e−4	−8.22e−6	3.08e−4	−5e−4	2.67e−4	0.15	0.0383	0.104	0.0443	−0.0692	−0.024	0.0181
0.11	−0.308	−0.448	−0.499	−0.451	0.317	−0.115	−0.455	−0.0136	0.239	0.222	−0.405	−0.167	0.14
9.94e−5	−7.34e−5	3.19e−4	6.74e−4	4.71e−4	1.36e−4	−2.44e−4	−0.157	−0.0215	0.0204	0.0667	−0.143	−0.0712	0.067
0.216	−0.486	−0.396	−0.0028	0.381	−0.488	0.221	−0.0943	−0.204	−0.706	−0.0867	−0.0912	−0.186	0.246
8.64e−5	0.00014	5.08e−4	−7.13e−7	−7.17e−4	2.86e−4	2.09e−4	0.13	−0.0125	−0.108	0.0125	−0.0995	−0.106	0.139
0.311	−0.45	0.106	0.499	0.119	0.448	−0.314	0.581	0.212	0.0369	−0.257	0.406	−0.0683	0.32
2.43e−5	1.39e−05	4.69e−05	−6.04e−5	−5.41e−5	−9.16e−5	7.14e−05	−0.0099	0.00299	0.0113	−0.0105	0.0248	−0.0954	0.225
0.39	−0.22	0.486	0.00468	−0.488	−0.207	0.394	−0.429	−0.343	0.45	0.188	0.475	0.169	0.365
4.84e−5	3.19e−4	−4.01e−4	−1.45e−5	0.00059	6.16e−4	1.07e−4	0.0536	−0.0918	0.0135	0.0898	0.0754	0.0736	0.0946
0.449	0.106	0.314	−0.499	0.306	−0.123	−0.452	0.0815	0.229	−0.242	0.309	0.0891	0.4	0.389
2.55e−5	2.06e−4	−4.67e−4	6.73e−4	−6.69e−4	−3.84e−4	−4.63e−5	−0.0294	0.0753	−0.0446	0.0881	0.041	0.191	0.194
0.487	0.39	−0.213	−0.00747	0.223	0.392	0.483	−0.247	0.339	−0.021	−0.366	−0.339	0.518	0.401
1.33e−4	1.61e−4	−2.12e−4	2.94e−4	−4.02e−4	−5.22e−4	−6.19e−4	0.00905	−0.0261	0.0192	−0.0699	−0.0732	0.325	0.295
0.503	0.505	−0.501	0.503	−0.506	−0.498	−0.497	0.358	−0.782	0.394	−0.765	−0.515	0.55	0.405

Appendix B

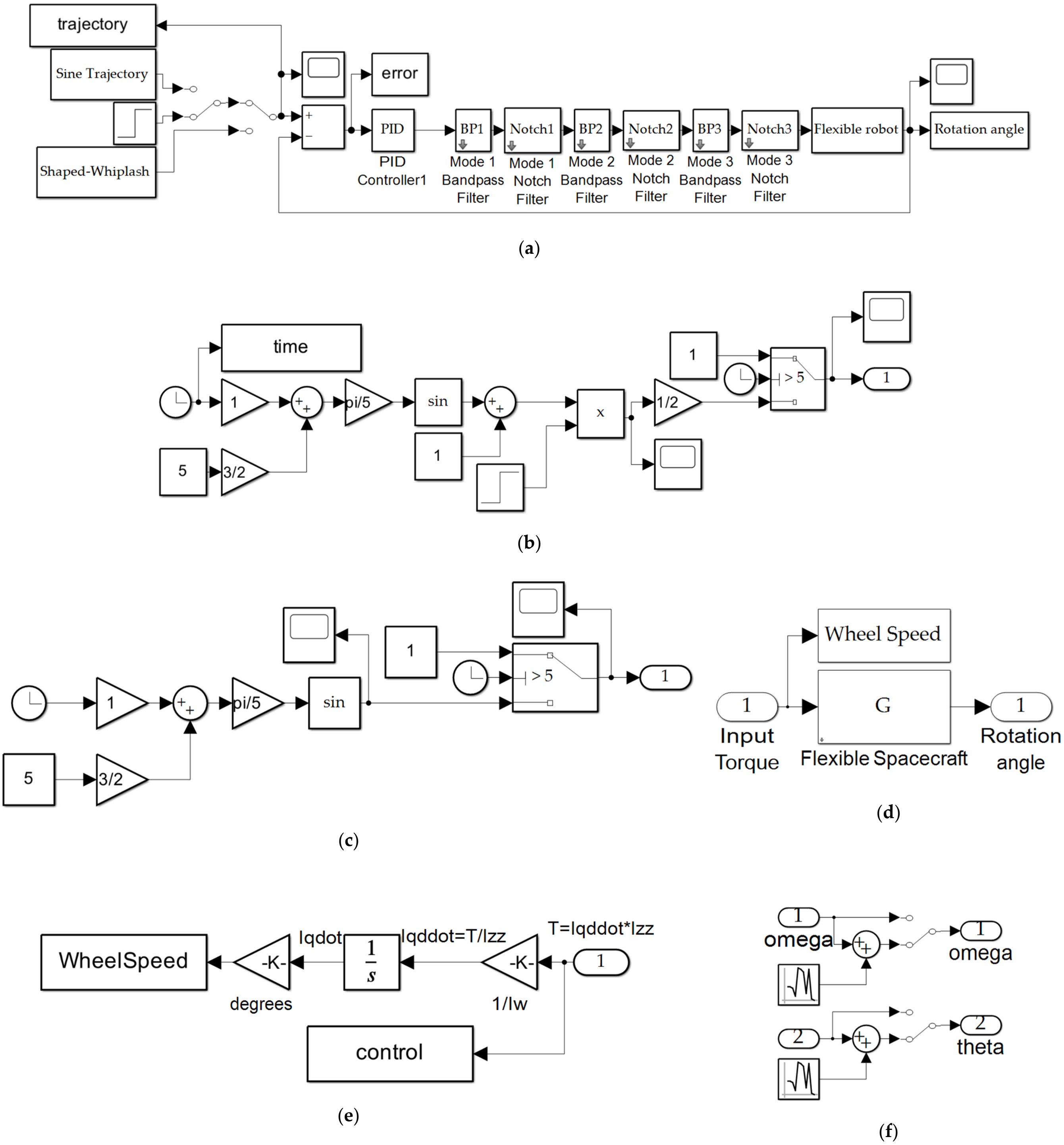

Figure A1. SIMULINK® models used to produce the results in this manuscript. (**a**) actuator reaction wheel simulation subsystem; (**b**) noisy sensor subsystem, (**c**) sinusoidal trajectory generation, (**d**) subsystem for flexible space robot, (**e**) conversion of wheel torque to display wheel speed, (**f**) sensor noise added to both angular state and rate measurements.

References

1. NASA Space Robotics Dive into Deep-Sea Work. Available online: https://www.nasa.gov/directorates/spacetech/spinoff/NASA_Space_Robotics_Dive_into_Deep_Sea_Work (accessed on 25 May 2023).
2. NASA Image Use Policy. Available online: https://gpm.nasa.gov/image-use-policy (accessed on 25 May 2023).
3. Tsiotras, P.; King-Smith, M.; Ticozzi, L. Spacecraft-Mounted Robotics. *Annu. Rev. Control. Robot. Auton. Syst.* **2023**, *6*, 335–362. [CrossRef]
4. Goddard Space Flight Center. *On-Orbit Satellite Servicing Study Project Report*; Goddard Space Flight Center, National Aeronautics and Space Administration: Greenbelt, MD, USA, 2010.
5. Wilde, M.; Harder, J.; Stoll, E. Editorial: On-orbit servicing and active debris removal: Enabling a paradigm shift in spaceflight. *Front. Robot. AI* **2019**, *6*, 136. [CrossRef]
6. Henry, C. FCC approves SpaceX, Telesat, LeoSat and Kepler internet constellations. *SpaceNews*, 15 November 2018.
7. Henry, C. Amazon planning 3236-satellite constellation for internet connectivity. *SpaceNews*, 4 April 2019.
8. Bronez, M.; Clarke, M.; Quinn, A. Requirements development for a free-flying robot—The "Robin". In Proceedings of the 1986 IEEE International Conference on Robotics and Automation, San Francisco, CA, USA, 7–10 April 1986.
9. Marvi, H. Opportunities and Challenges in Space Robotics. *Adv. Intell. Syst.* **2023**, *5*, 2200277. [CrossRef]
10. Sands, T. Flattening the Curve of Flexible Space Robotics. *Appl. Sci.* **2022**, *12*, 2992. [CrossRef]
11. Sands, T. Optimization Provenance of Whiplash Compensation for Flexible Space Robotics. *Aerospace* **2019**, *6*, 93. [CrossRef]
12. Kwatny, H.; Baek, M.; Bennett, W.; Blankenship, G. Attitude Control of Articulated, Flexible Spacecraft. *IFAC Proc. Vol.* **1992**, *25*, 463–469. [CrossRef]
13. Gutiérrez, G. Design, Implementation and Evaluation of Control Strategies Targeting Flexible Structures in the Space Domain, Based in an Analytical Modeling of These Structures. Master of Science Thesis, Delft University of Technology, Delft, The Netherlands, 22 January 2019. Available online: https://elib.dlr.de/126439/1/Gutierrez%20-%20Attitude%20control%20of%20flexible%20spacecraft.pdf (accessed on 25 May 2023).
14. Colagrossi, A.; Lavagna, M. Integrated vibration suppression attitude control for flexible spacecrafts with internal liquid sloshing. *Multibody Syst. Dyn.* **2021**, *51*, 123–157. [CrossRef]
15. Wei, C.; Gu, H.; Liu, Y.; Zhao, Y. Attitude reactionless and vibration control in space flexible robot grasping operation. *Int. J. Adv. Robot. Syst.* **2018**, *15*, 1–10. [CrossRef]
16. Kraiem, S.; Rognant, M.; Biannic, J.; Briere, Y. Control of rotation-floating space robots with flexible appendages for on-orbit servicing. In Proceedings of the 2021 European Control Conference (ECC), Rotterdam, The Netherlands, 29 June–2 July 2021; pp. 249–254.
17. Shahravi, M.; Azimi, M. Attitude and Vibration Control of Flexible Spacecraft Using Singular Perturbation Approach. *Int. Sch. Res. Not.* **2014**, *13*, 163870. [CrossRef]
18. Yang, B.; Wang, W.; Meng, H.; Wan, W.; Bao, G. Monitoring and Control of Position and Attitude of Flexible Manipulator with Three Degrees of Freedom. In Proceedings of the 4th IEEE International Conference on Advanced Robotics and Mechatronics (ICARM), Toyonaka, Japan, 3–5 July 2019; pp. 208–213.
19. Mahdi, S.M.; Yousif, N.Q.; Oglah, A.A.; Sadiq, M.E.; Humaidi, A.J.; Azar, A.T. Adaptive Synergetic Motion Control for Wearable Knee-Assistive System: A Rehabilitation of Disabled Patients. *Actuators* **2022**, *11*, 176. [CrossRef]
20. Spacecraft Research & Design Center. Available online: https://nps.edu/web/srdc/laboratories (accessed on 25 May 2023).
21. Use of Department of Defense Imagery. Available online: https://www.defense.gov/Contact/Help-Center/Article/Article/2762906/use-of-department-of-defense-imagery/ (accessed on 25 May 2023).
22. Copyrights. Available online: https://www.mdpi.com/authors/rights#:~:text=All%20articles%20published%20by%20MDPI,MDPI,%20including%20figures%20and%20tables (accessed on 25 May 2023).
23. Electronics Tutorials: Second Order Filters. Available online: https://www.electronics-tutorials.ws/filter/second-order-filters.html (accessed on 20 December 2023).